*Sensors and Materials*, Vol. 36, No. 5 (2024) 1859–1868
MYU Tokyo


S & M 3640

# Microheaters for Thermal Analysis and Gas Sensing Applications

Bo-Ming Huang,[1] Yu-Jen Hsiao,[2*] Sheng-Chang Wang,[1] and Meichun Lin[3]

[1]Department of Mechanical Engineering, Southern Taiwan University of Science and Technology, No. 1, Nantai St., Yungkang Dist., Tainan City 710301, Taiwan
[2]Department of Vehicle Engineering, National Kaohsiung University of Science and Technology, Kaohsiung 824005, Taiwan
[3]Department of Finance and International Business, Fu Jen Catholic University, New Taipei City 242062, Taiwan

(Received October 30, 2023; accepted April 17, 2024)

***Keywords:*** MEMS, microheater, ANSYS, gas sensor

In this study, we primarily focus on the design and fabrication of microheaters for bottom-heating applications combined with gas sensing. Our main objectives are to analyze energy consumption and temperature distribution, utilizing this microheater component for development and simulation. In the design of microheaters, we employ finite element analysis using Analysis System (ANSYS) to simulate the geometric designs of microheaters. The results obtained, which reveal the temperature distribution within a 400 μm² region at 300 °C, provide insights into the temperature distribution on the sensing membrane. The fabrication is carried out using MEMS technology, followed by validation. Furthermore, sensitivity testing is performed on gas sensors for volatile organic compounds in the range from 0.2 to 1 ppm, resulting in an increase from 12.2 to 89.7%.

## 1. Introduction

In the current era of rapid technological advancement, heating technology has become a critical component in various fields such as science, engineering, and aviation. Its primary objective is to provide precise temperature control to create an optimal heating environment for equipment. However, traditional heating methods, such as heating plates or Peltier elements, suffer from bulky dimensions and low conversion efficiency, limiting the applicability of the technology. Therefore, miniaturization has emerged as the prevailing trend. To achieve the goal of miniaturization, technological innovations are required, including the development of novel materials, enhancements in heating element design, and the adoption of more efficient heat transfer methods. Among these, improving conversion efficiency and reducing energy consumption are key challenges. Additionally, precise temperature control technology is crucial in ensuring the stability and reliability of heaters.[1,2]

In the field of gas sensing, gas sensors based on MEMS technology have attracted significant research and application interest owing to their acceptable sensitivity, low cost, production flexibility, stability, and applicability over a wide range of operating temperatures. These sensors

*Corresponding author: e-mail: yujen@nkust.edu.tw
https://doi.org/10.18494/SAM4804

ISSN 0914-4935 © MYU K.K.
https://myukk.org/

find applications in areas such as environmental monitoring, healthcare, the food industry, industrial processes, and toxic gas detection. In these applications, microheaters play a vital role as they are responsible for controlling the temperature of the sensing membrane.

During gas sensing, a semiconductor chemical resistance film must be heated to a specific temperature to create a depletion layer by adsorbing oxygen atoms, which enables the detection of the concentration of reducing gases. This change is reflected in the resistance values. To monitor these resistance changes, the temperature of the microheater must be kept constant and uniform across the entire heater region. To achieve this, microheaters manufactured using MEMS technology can improve the dynamic response of the sensing process and reduce energy consumption.

The aim of this paper is to design, simulate,[3] and evaluate the performance of low-energy microheaters for gas sensors, ensuring that the sensor's operating temperature can reach the required range while maintaining its reliability. To optimize the structure of microheaters, different geometric shapes, sizes, and materials of heating electrodes will be considered, and temperature distribution and energy consumption will be simulated. After simulating various microheaters, the selected designs will be developed and validated using thermal imaging equipment for energy analysis.

## 2. Materials and Methods

In this study, the nodes of the microheater are considered to form a 2D plane. To acquire temperature distributions at different locations within the microheater, calculations are carried out using nodes and the 2D heat conduction equation. The general formula for heat diffusion in a Cartesian coordinate system is expressed as

$$\frac{\partial}{\partial x}\left(k\frac{\partial T}{\partial x}\right)+\frac{\partial}{\partial y}\left(k\frac{\partial T}{\partial y}\right)+\frac{\partial}{\partial z}\left(k\frac{\partial T}{\partial z}\right)+\dot{q}=\rho c_p\frac{\partial T}{\partial t}. \tag{1}$$

This formula elucidates the fundamental principles of heat conduction analysis. As it is treated from a 2D standpoint, temperature changes along the $Z$-axis, $\partial/\partial z(k\partial T/\partial z)$, are deemed negligible. Additionally, the simulations are performed under steady-state conditions; thus, the time derivatives of density and specific heat, $\rho c_p\, \partial T/\partial t$, are also excluded from consideration. Assuming a constant thermal conductivity ($k$), the equation is then represented as

$$\frac{\partial^2 T}{\partial x^2}+\frac{\partial^2 T}{\partial y^2}+\frac{\dot{q}}{k}=0. \tag{2}$$

Subsequently, by the energy balance method, finite difference equations for nodes are derived using the principle of energy conservation, describing the control volume within the node region. Therefore, this equation can be expressed as

$$\left(\frac{\partial^2 T(x,y)}{\partial x^2}+\frac{\partial^2 T(x,y)}{\partial y^2}\right)+\frac{\dot{q}}{k}(\Delta x\cdot\Delta y)=0. \tag{3}$$

In Eq. (3), '$x$' and '$y$' represent the two directions of the Cartesian coordinate system, $\dot{q}/k$ denotes the heat generation, and $T(x, y)$ represents the temperature at the spatial coordinates ($x_m$, $y_n$). By substituting the spatial coordinates ($x_m$, $y_n$) into the equation, the differential forms along the $x$- and $y$-axes are expressed as

$$\frac{\partial^2 T(x,y)}{\partial x^2}\approx\frac{T(x+\Delta x,y)-2T(x,y)+T(x-\Delta x,y)}{(\Delta x)^2}, \tag{4}$$

$$\frac{\partial^2 T(x,y)}{\partial y^2}\approx\frac{T(x,y+\Delta y)-2T(x,y)+T(x,y-\Delta y)}{(\Delta y)^2}. \tag{5}$$

By substituting Eqs. (4) and (5) into Eq. (3), assuming $\Delta x = \Delta y$, and then simplifying, the resulting 2D heat conduction difference equation can be expressed as

$$\frac{T(x+\Delta x,y)-2T(x,y)+T(x-\Delta x,y)}{(\Delta x)^2}+\frac{T(x,y+\Delta y)-2T(x,y)+T(x,y-\Delta y)}{(\Delta x)^2}+\frac{\dot{q}(\Delta x)^2}{k}=0. \tag{6}$$

After rearranging Eq. (6), the discrete representation of 2D heat conduction can be expressed as

$$T_{m,n+1}+T_{m,n-1}+T_{m+1,n}+T_{m-1,n}+\frac{\dot{q}(\Delta x)^2}{k}-4T_{m,n}=0. \tag{7}$$

Owing to the intricate geometric configuration of the microheater discussed in this paper, the calculations are conducted utilizing the discrete form of 2D heat conduction. The temperature is obtained through heat conduction to an interior node from its adjoining nodes, as depicted in Fig. 1.[4]

In this study, we employed Analysis System (ANSYS) simulation software for simulation modeling, as shown in Fig. 2. First, it is necessary to select the analysis type. Given that we focus on simulating a microheater with a structural design falling under the thermoelectric category, we have opted for thermoelectric simulation analysis. Subsequently, we proceed to creating the geometric model, either by drawing or importing it. In this paper, we have chosen to import

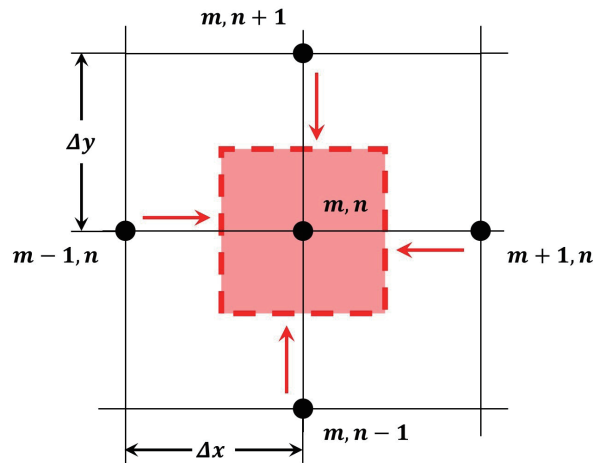


Fig. 1. (Color online) Conduction to an interior node from its adjoining nodes.

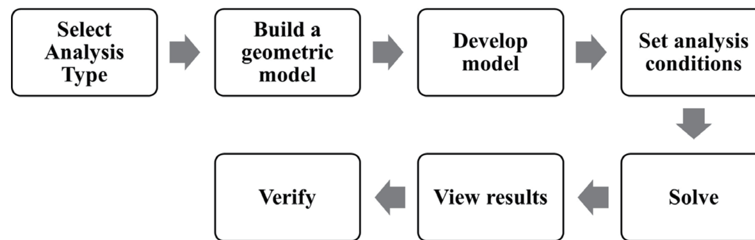


Fig. 2. ANSYS simulation process.

image files as outlined in Fig. 3. We have designed 3D gas sensors of the straight-line type. The reason for increasing the line width of the heater from 15 µm at the center outward is that, under constant thickness, smaller line widths lead to a more challenging current conduction, resulting in rapid heating. However, this also increases energy consumption. Therefore, this design is employed to reduce energy consumption.[5–7]

After establishing the geometric model of the microheater, the next step is model development, which includes defining materials and creating a mesh. In this paper, we utilized ANSYS' internal tool, Engineering Data, for material properties,[8–14] as indicated in Table 1. Subsequently, the corresponding materials will be defined within the geometric model. Following this, a mesh will be applied to partition the geometric model.

Once the model development is completed, the analysis conditions should be set, including constraints and loads. On the basis of the analysis type, various loads, such as thermal or electrical loads, can be applied. Consequently, we gradually applied electrical current to the microheater structure, increasing by 5 mA at each step, and also applied thermal convection (200 W/m$^2$K) at an ambient temperature of 22 °C as the analysis conditions. Subsequently, the solution phase follows, employing temperature and voltage solvers. This choice is made because it is necessary to understand the temperature distribution and voltage produced under these analysis conditions for observation. Subsequently, experimental validation is conducted.

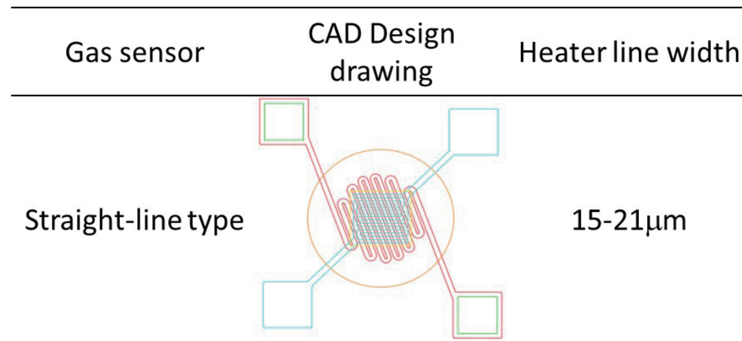


Fig. 3. (Color online) 3D structure gas sensor design drawing.

Table 1
Simulated material property parameters.

| Material | Si | $SiO_2$ | $Si_3N_4$ | Ti | Pt | $SnO_2$ | Al |
|---|---|---|---|---|---|---|---|
| Density (kg/m$^3$) | 2330 | 2220 | 2400 | 4500 | 21450 | 6950 | 2689 |
| Coefficient of thermal expansion (°C) | $3.61 \times 10^{-6}$ | $5.00 \times 10^{-7}$ | $2.80 \times 10^{-6}$ | $8.90 \times 10^{-6}$ | $9.10 \times 10^{-6}$ | $7.10 \times 10^{-6}$ | $2.55 \times 10^{-5}$ |
| Young's modulus (pa) | $1.12 \times 10^{11}$ | $7.00 \times 10^{10}$ | $2.90 \times 10^{7}$ | $1.15 \times 10^{11}$ | $1.72 \times 10^{11}$ | $5.59 \times 10^{10}$ | $6.80 \times 10^{10}$ |
| Poisson's ratio | 0.28 | 0.16667 | 0.25 | 0.34 | 0.39 | 0.27 | 0.36 |
| Bulk modulus (pa) | $8.51 \times 10^{10}$ | $3.50 \times 10^{10}$ | $1.93 \times 10^{7}$ | $1.20 \times 10^{11}$ | $2.61 \times 10^{11}$ | $4.05 \times 10^{10}$ | $8.10 \times 10^{10}$ |
| Shear modulus (pa) | $4.39 \times 10^{10}$ | $3.00 \times 10^{10}$ | $1.16 \times 10^{7}$ | $4.30 \times 10^{10}$ | $6.20 \times 10^{10}$ | $2.20 \times 10^{10}$ | $2.50 \times 10^{10}$ |
| Thermal conductivity (W/m·C) | 148 | 1.5 | 16 | 21 | 72 | 27.4 | 210 |
| Specific heat (J/kg·C) | 712 | 745 | 691 | 552 | 133 | $2.27 \times 10^{-4}$ | 951 |
| Resistivity (Ω·cm) | 0.01 | NA | NA | $5.54 \times 10^{-5}$ | $1.06 \times 10^{-5}$ | 7140 | $2.70 \times 10^{-6}$ |

The 3D gas sensors used in this study were all manufactured by MEMS fabrication. The fabrication process consists of five distinct steps, as shown in Fig. 4.

- Supporting layer (Si, $SiO_2$, $Si_3N_4$): Initially, a 1000-nm-thick $SiO_2$ layer and a 300-nm-thick $Si_3N_4$ layer were deposited on a silicon (Si) substrate by a high-temperature, high-pressure furnace process. Subsequently, chemical-mechanical polishing was employed to reduce the Si substrate thickness from 600 to 400 μm, followed by a polishing step.
- Heating electrodes (Ti, Pt): Next, a 300-nm-thick layer of titanium (Ti) and a 300-nm-thick layer of platinum (Pt) were deposited onto the substrate to form the heating electrodes.
- Insulating layer ($SiO_2$): A 700-nm-thick $SiO_2$ layer was deposited as an insulating layer by plasma-enhanced chemical vapor deposition. This insulating layer prevents the unintended electrical conduction between the sensing and heating electrodes.
- Sensing electrodes (Ti, Pt): Similar to the heating electrodes, a 300-nm-thick layer of Ti and a 300-nm-thick layer of Pt were deposited to form the sensing electrodes.
- Sensing layer ($SnO_2$) and barrier layer (Al): A 700-nm-thick layer of tin dioxide ($SnO_2$) is deposited on top of the sensing electrode through radio frequency sputtering, followed by annealing at 500 °C for 10 min. Subsequently, a 500-nm-thick aluminum layer was deposited on the back side of the substrate as a barrier layer.

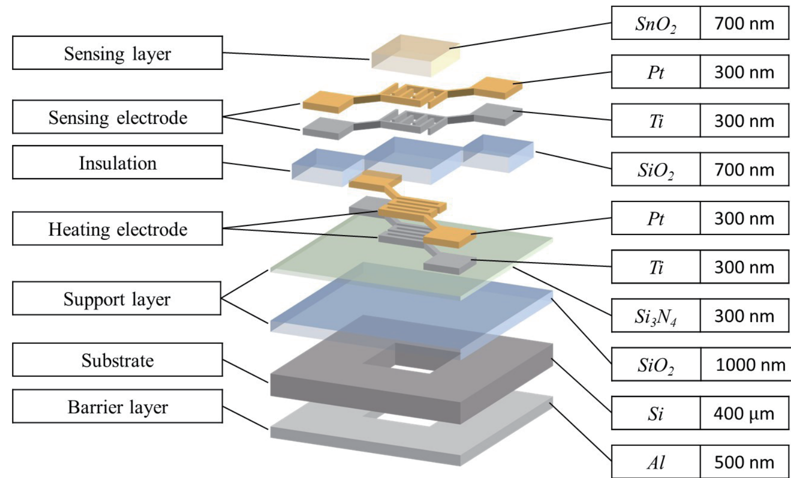


Fig. 4. (Color online) Schematic of 3D structure gas sensor.

The final step involves inductively coupled plasma etching performed to selectively remove a material where there is no barrier layer. This process is intended to prevent the dissipation of heat generated by the electrodes through the silicon substrate, thereby improving the energy efficiency of microheaters and concentrating heat within the gas sensor.

## 3. Results and Discussion

MEMS microheater elements play a vital role in semiconductor gas sensors. In this study, the design of the back opening was used to meet the demand for improving energy efficiency, and a 3D laser microscope was used to measure the surface profile. The 3D laser microscope has five sets of laser-specific objective lenses, namely, 5×, 10×, 20×, 50×, and 100× lenses. As shown in Fig. 5, 10× is used to measure the surface profile height. Subsequently, the heating performance of microheaters, especially 3D microheaters, was studied. The structure of the sensor after fabrication is shown in Fig. 6. The sensor was then placed under the lens of a thermal imaging camera and tested at temperatures from 50 to 300 ℃ to evaluate its heating efficiency.

By increasing the electrical current to heat the sensors, the power can be calculated using Eq. (8). Furthermore, the actual temperature of the sensors was visualized using a thermal imaging device, enabling the observation of their heating power curves.

$$P(\mathrm{mW}) = VI \tag{8}$$

As shown in Fig. 7, the power consumption curves of samples A to D were analyzed, including actual and simulated curves. A power supply was used to provide current to gradually heat up the microheater, and it was observed with a thermal imager. It was observed that sample C showed a significantly lower power of about 61.2 mW when the temperature reached 300 ℃. Then, the resistance of the $SnO_2$ sensing film before heating was 310 Ω, and it was 1 kΩ when the temperature reached 300 ℃. Subsequently,

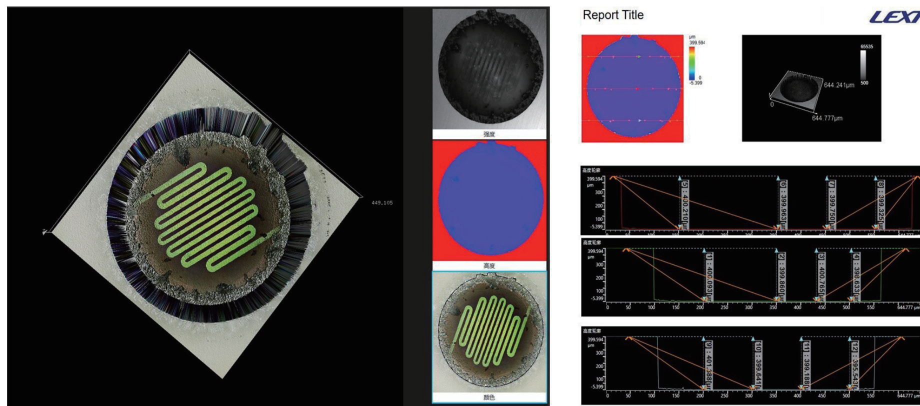


Fig. 5. (Color online) Back etching.

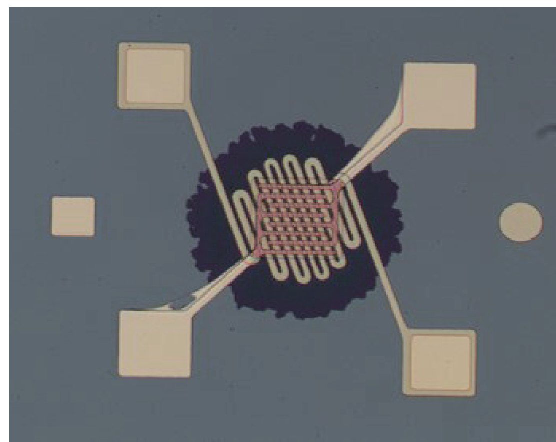

Fig. 6. (Color online) Completed drawing of 3D structure gas sensor.

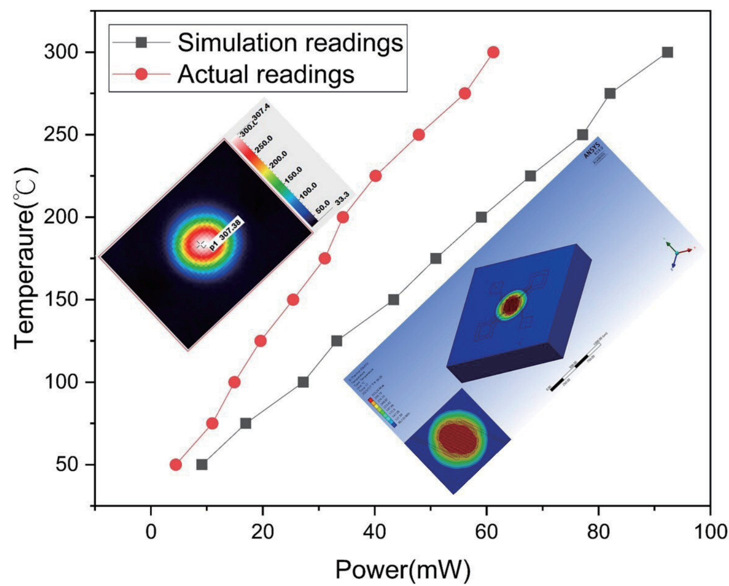


Fig. 7. (Color online) Thermal imager and simulation and temperature and power consumption curves.

measurements were conducted on gas sensors coated with $SnO_2$ thin films within the temperature range from 150 to 250 ℃. The testing results indicated that the optimal operating temperature for $SnO_2$ measurements was 200 ℃.

Gas sensing responses were tested in a glass chamber where the MEMS microheater is connected to a resistance meter and a heating source through sensing and heating electrodes. When VOC gas is introduced into the chamber, the resistance of the sensor changes considerably, and the change in resistance is used to calculate the sensing response of the VOC gas. Five different variations of VOC gas concentrations were tested as shown in Fig. 8. At 0.2 ppm, the sensor reached 15% response, and as the sensing response increased to 1 ppm, the sensor exhibited 90% response. The analysis results showed that the sensor has good response and recovery times with stable sensor resistances in the presence of air and VOC gas. The optimal operating temperature for these measurements was determined to be 200 ℃. On the basis of the change in resistance, the gas sensing response was measured as

$$\text{Gas sensing response (\%)} = \left| \frac{R_{gas} - R_{air}}{R_{gas}} \right| \times 100\%. \tag{9}$$

During the gas testing procedure, the calculated response was observed to be 12.2% at 0.2 ppm, 28.4% at 0.4 ppm, 43.9% at 0.6 ppm, 64.7% at 0.8 ppm, and 89.7% at 1 ppm, as illustrated in Fig. 8. This indicates a favorable level of response for the sensor.(15–18)

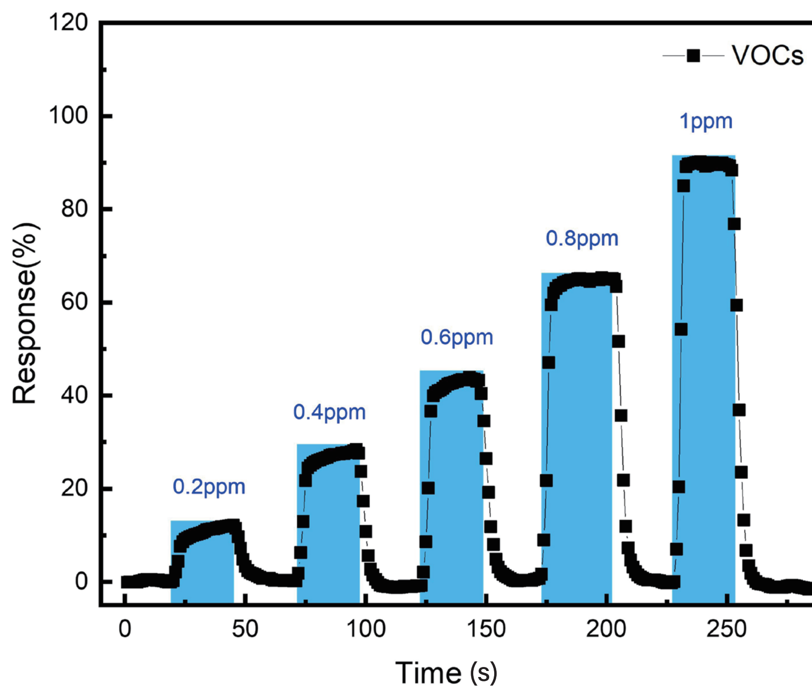


Fig. 8. (Color online) Gas continuous response.

## 4. Conclusion

We mainly focused on the application of microheaters for gas sensors and related studies. We employed ANSYS finite element analysis to simulate geometrically designed heating electrodes and established simulation conditions, including thermal conductivity coefficients, specific heat coefficients, and material densities for each layer. The subsequent development and design were all based on the MEMS process. We carried out electrical-thermal simulation to analyze heating electrodes with different geometric designs. The maximum temperature of the microheater can reach 300 ℃. During gas measurements, the microheater can detect 0.2 ppm of volatile organic compound gases at 200 ℃, with a sensitivity of 12.2%.

## Acknowledgments

This study is supported by the Ministry of Science and Technology under project nos. NSTC 112-2218-E-992-006 -MBK and NSTC 112-2221-E-992-100. We would like to thank the Taiwan Semiconductor Research Institute (TSRI) for providing the MEMS sensor devices and Ms. Hui-Jung Shih of the core center facility of National Cheng Kung University for the use of high-resolution SEM (HITACHI SU8000).

## References

1 P. Bhattacharyya: IEEE Trans. Device Mater. Reliab. **14** (2014) 589. https://doi.org/10.1109/TDMR.2014.2311801
2 Z. E. Jeroish, K. S. Bhuvaneshwari, F. Samsuri, and V. Narayanamurthy: Biomed. Microdevices **24** (2022) 1. https://doi.org/10.1007/s10544-021-00595-8
3 S. Astié, A. M. Gué, E. Scheid, L. Lescouzères, and A. Cassagnes: Sens. Actuators, A **69** (1998) 205. https://doi.org/10.1016/S0924-4247(98)00096-X
4 F. P. Incropera: Fundamentals of Heat and Mass Transfer, D. P. DeWitt, T. L. Bergman, and A. S. Lavine, Eds. (John Wiley & Sons, New Jersey, 2006) 6th ed., Chap. 4.
5 S. Yu, S. Wang, M. Lu, and L. Zuo: Sens. Actuators, A **257** (2017) 58. https://doi.org/10.1016/j.sna.2017.02.006
6 M. Baroncini, P. Placidi, G. C. Cardinali, and A. Scorzoni: Sens. Actuators, A **115** (2004) 8. https://doi.org/10.1016/j.sna.2004.03.012
7 G. Velmathi, N. Ramshanker, and S. Mohan: IECON 2010 36th Ann. Conf. IEEE Industrial Electronics Society (IEEE, 2010) 1258.
8 R. M. Tiggelaar, R. G. Sanders, A. W. Groenland, and J. G. Gardeniers: Sens. Actuators, A **152** (2009) 39. https://doi.org/10.1016/j.sna.2009.03.017
9 D. D. Lee, W. Y. Chung, M. S. Choi, and J. M. Baek: Sens. Actuators, B **33** (1996) 147. https://doi.org/10.1016/0925-4005(96)01822-9
10 G. Sberveglieri, W. Hellmich, and G. Müller: Microsyst. Technol. **3** (1997) 183. https://doi.org/10.1007/s005420050078
11 A. Götz, I. Gràcia, C. Cané, and E. Lora-Tamayo: J. Micromech. Microeng. **7** (1997) 247. https://doi.org/10.1088/0960-1317/7/3/045
12 C. Rossi, P. Temple-Boyer, and D. Estève: Sens. Actuators, A **64** (1998) 241. https://doi.org/10.1016/S0924-4247(97)01627-0
13 C. Rossi, E. Scheid, and D. Esteve: Sens. Actuators, A **63** (1997) 183. https://doi.org/10.1016/S0924-4247(97)80503-1
14 I. Simon, N. Bârsan, M. Bauer, and U. Weimar: Sens. Actuators, B **73** (2001) 1. https://doi.org/10.1016/S0925-4005(00)00639-0
15 S. J Young and Y. L. Chu: IEEE Trans. Electron Devices **68** (2021) 1886. https://doi.org/10.1109/TED.2021.3060354

16 S. J. Young and Y. L. Chu: J. Electrochem. Soc. **167** (2020) 1. https://doi.org/10.1149/1945-7111/abc4be
17 Y. L. Chu, S. J. Young, L. W. Ji, T. T. Chu, K. T. Lam, Y. J. Hsiao, I. T. Tang, and T. H. Kuo: J. Electrochem. Soc. **167** (2020) 1. https://doi.org/10.1149/1945-7111/aba00d
18 Y. H. Liu, S. J. Chang, L. T. Lai, Y. P. Tu, and S. J. Young: Microsyst. Technol. **28** (2022) 377. https://doi.org/10.1007/s00542-020-04856-z


## About the Authors

**Bo-Ming Huang** received his B.S. and M.S. degrees from Southern Taiwan University of Science and Technology (STUST) in 2021 and 2023, respectively. He is currently pursuing his Ph.D. degree in the field of micro and nano gas sensing technology at STUST. His research interests include MEMS, simulation, and gas sensors. (DB21Y204@stust.edu.tw)

**Yu-Jen Hsiao** received his B.S. M.S., and Ph.D. degrees from the Department of Materials Science and Engineering, National Cheng Kung University, in 1999, 2001, and 2007, respectively. He was a professor at National Kaohsiung University of Science and Technology, Taiwan. His research interests are in MEMS sensor, semiconductor component manufacturing, and system integration. (yujenhsiao.tw@gmail.com)

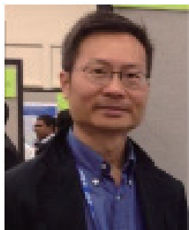

**Sheng-Chang Wang** received his B.S. degree from Feng Chia University, Taiwan, in 1992 and his M.S. and Ph.D. degrees from National Taiwan University, Taiwan, in 1997 and 2001, respectively. From 2014 to 2018, he was a professor and the Director of the Nanotechnology Research Center at Southern Taiwan University of Science and Technology, Taiwan. Since 2018, he has been a professor and the Chairman of the Department of Mechanical Engineering of Southern Taiwan University of Science and Technology, Taiwan. His research interests are in nanomaterials for energy applications, ceramic processing, TEM analyses, and electrophoretic deposition.
(scwang@stust.edu.tw)

**Mei-Chun Lin** received her M.S. degree from Northumbria University, UK in 2004 and her Ph.D. degree from the Department of Industrial and Information Management, National Cheng Kung University, Taiwan in 2019. From 2021 to 2023, she was an assistant professor in the Department of Finance and International Business at Fu Jen Catholic University, Taiwan. Her research interests are in manufacturing and information system integration, digital transformation, and ESG supply chain management.
(151308@mail.fju.edu.tw)